Electronic Supplementary Material (ESI) for Journal of Materials Chemistry A.

Supporting Information

Template-free synthesis of boron nitride foam-like porous monoliths and their high-end applications in water cleaning

Yanming Xue[†,*], Pengcheng Dai[╫,*], Xiangfen Jiang[†], Xuebin Wang[†], Chao Zhang[†,‡], Daiming Tang[†], Qunhong Weng[†], Xi Wang[†], Amir Pakdel[†], Chengchun Tang[‖,⊥,*], Yoshio Bando[†] and Dmitri Golberg[†,‡,*]

[†] *International Center for Materials Nanoarchitectonics (MANA), National Institute for Materials Science (NIMS), Namiki 1, Tsukuba, Ibaraki 3050044, Japan*

[╫] *Research Institute of Unconventional Petroleum and Renewable Energy, China University of Petroleum (East China), Qingdao 266580, P.R. China*

[‖] *School of Materials Science and Engineering, Hebei University of Technology, Tianjin, 300130, P.R. China*

[⊥] *Hebei Key Laboratory of Boron Nitride Micro- and Nano-Materials, Tianjin 300130, P.R. China*

[‡] *University of Tsukuba, Tennodai 1, Tsukuba, Ibaraki 3050005, Japan*

Content

1.

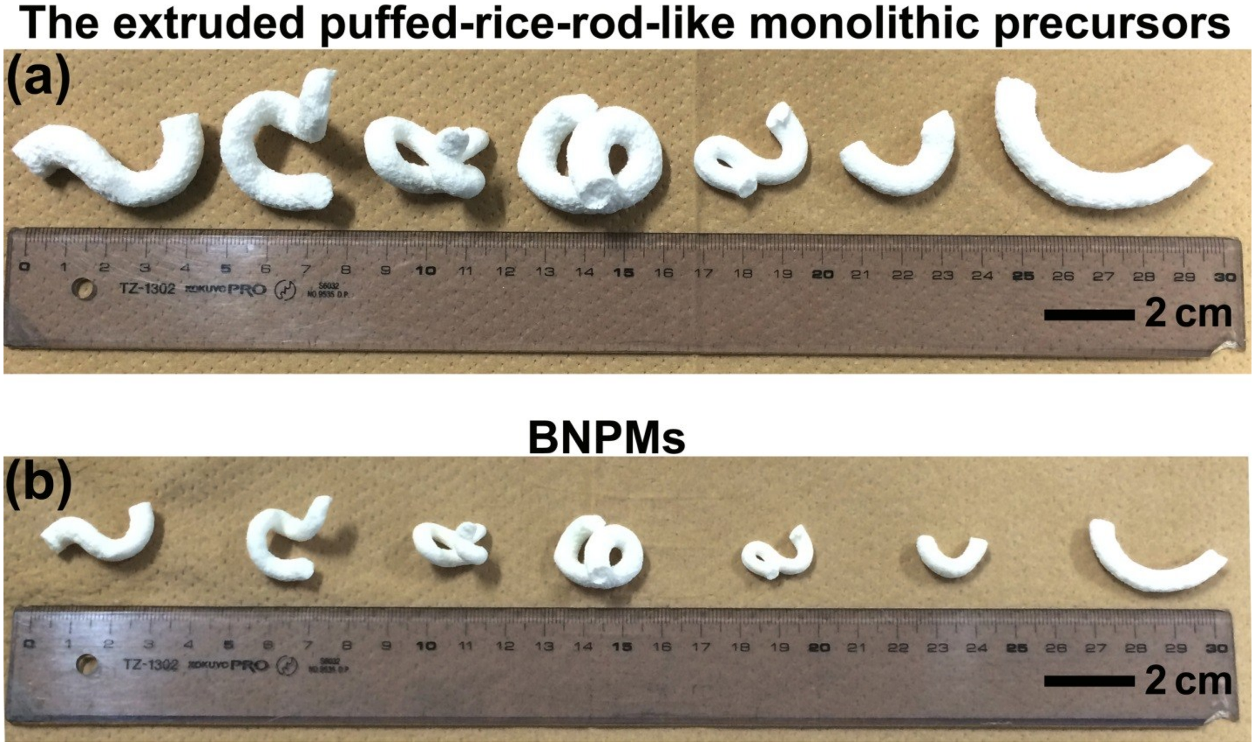

Figure S1. The photographs of the monolithic precursors and BNPMs. (a) The extruded puffed-rice-rod-like monolithic precursors. (b) The BNPMs obtained from pyrolyzing of the extruded puffed-rice-rod-like monolithic precursors with ammonia flow at 1100 °C.

2.

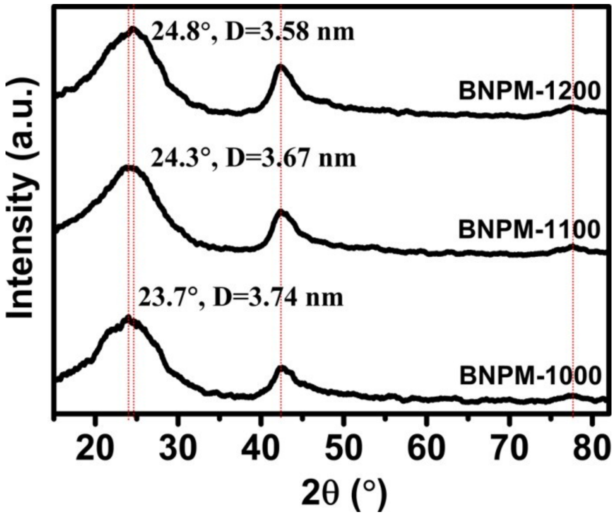

Figure S2. XRD patterns of BNMPs obtained at 1000, 1100 and 1200 °C (corresponding to the sample notations of BNPM-1000, BNPM-1100 and BN-1200), by using Cu Kα radiation.

All the white-colored BNPM samples prepared at 1000, 1100 and 1200 °C reveal a typical hexagonal structure of BN, which shows primary two broad diffraction peaks centered at ~ 23.7-24.8° and ~ 42.3° and a weak diffraction peak located at about 77.2°. They are indexed to the (002) and (100) planes of h-BN and its (110) plane. The (002) interplanar distance of traditional bulk h-BN has been reported to be ~ 0.33-0.34 nm [S1], and the as-measured (002) in-plane lattice spacings of all the as-obtained BNPM samples are larger than 0.35 nm. The well-known turbostratic BN (t-BN) materials have a (002) plane distance value of ~ 0.356 nm [S2]. Another ordering type of BN is its amorphous-likestructure, which usually has no obvious reflections in XRD patterns, but a very broad diffraction peak located at the vicinity of the (002) reflection of h-BN [S3]. Based on the XRD in Figure S1, it means that the BNPMs possess a typical ordering type of t-BN that is an intermediate phase between the classical bulk h-BN and amorphous BN. The t-BN does not have a peculiar crystal structure (this can be confirmed by the corresponding TEM described in the main text). In general, the lattice constants of such BN are determined by a reference to h-BN, and indexed according to the diffraction analyses of well-defined h-BN. The obvious broadening of the (002) reflection is caused by the layer-disordered turbostratic features of h-BN [S4]. With an increase in the synthesis temperature, the XRD (002) reflections of the products slightly move to right, leading to d(002) values decrease from 3.74 nm to 3.58 nm. This indicates that the turbostratic structures would be improved towards a well-crystalized h-BN.

3.

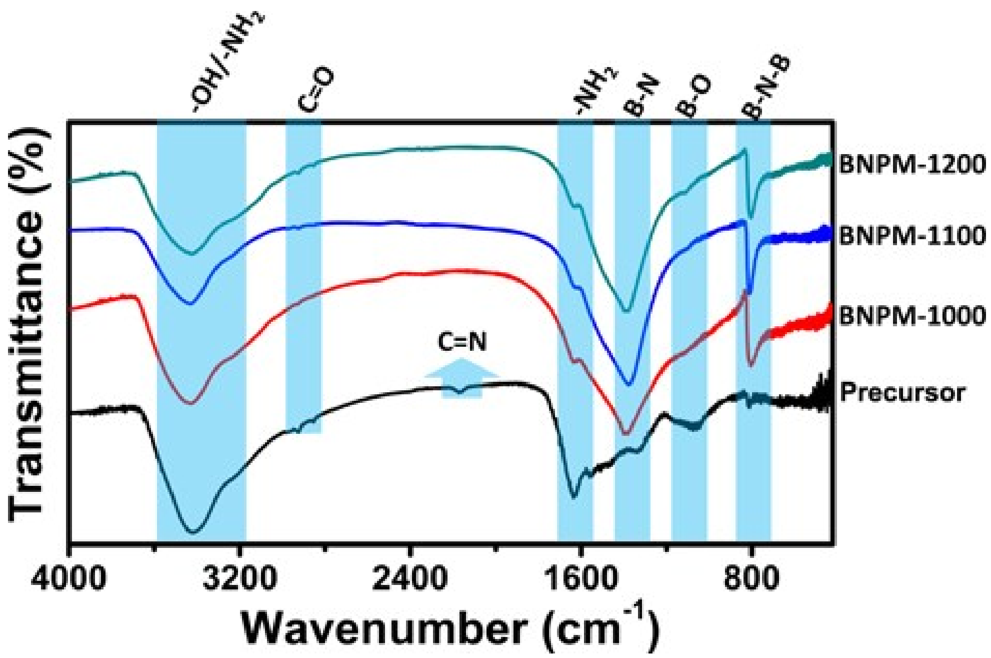

Figure S3. FTIR spectra of BNPM samples and a monolithic precursor.

4.

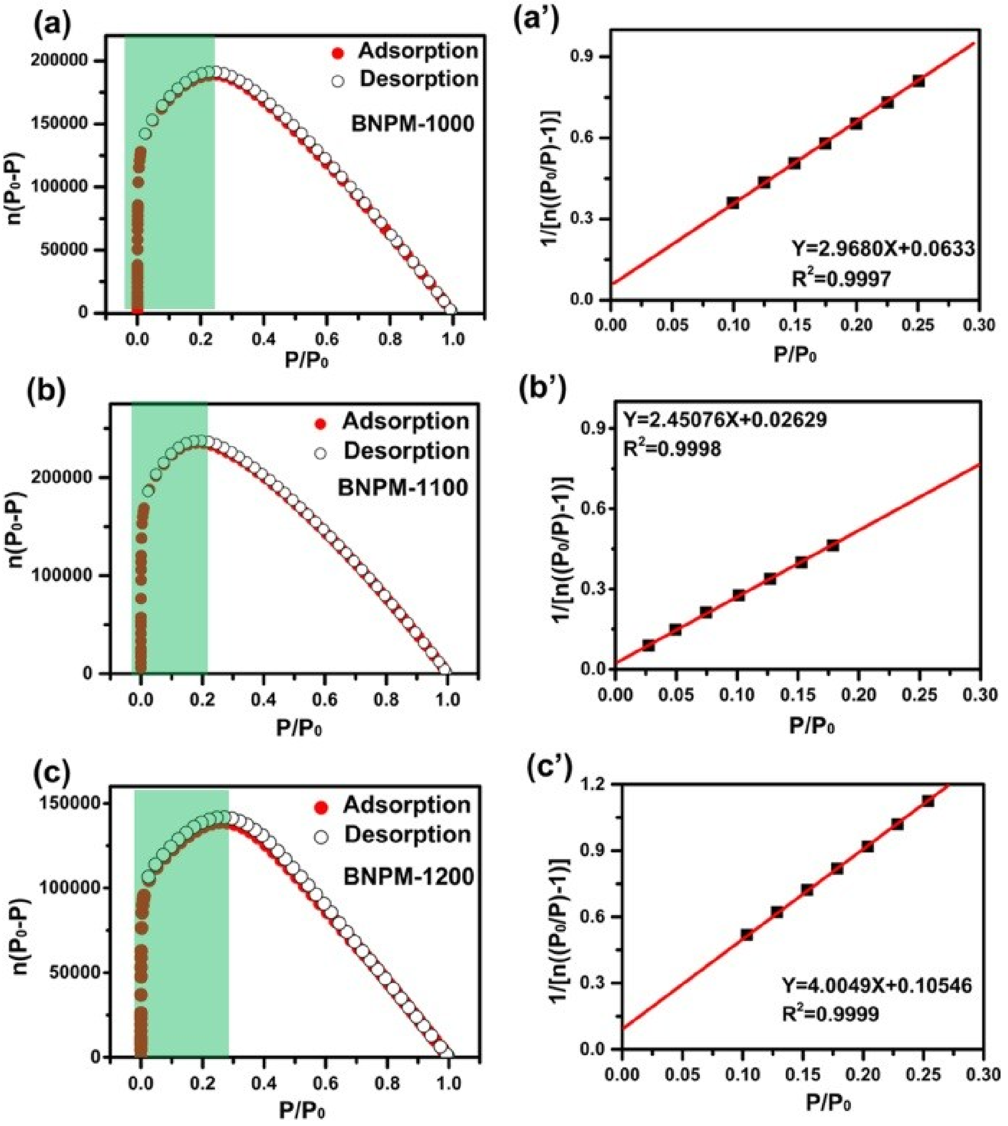

Figure S4. $n(P_0\text{-}P)$ vs P/P_0 plots of BNPM samples based on N_2 adsorption-desorption isotherm: a) BNPM-1000; b) BNPM-1100; c) BNPM-1200. Corresponding seven-point BET plots in the selected reasonable pressure range of the adsorption-desorption data from BNPM samples: a') BNPM-1000; b') BNPM-1100; c') BNPM-1200.

The BET SSA calculation evaluation requires a linear relationship between the $1/[n(P_0/P)\text{-}1]$ and P/P_0, meanwhile, the linear plot must possess a positive value in *y*-intercept. In addition, the BET equation needs to limit the pressure range in order to satisfy a condition that the term n(P_0-P) monotonically increases with the P/P_0 (here, *n* is the adsorbed N_2 amount (cc/g)). Based on such strict criteria, the P/P0 ranges can be selected in Figure S4 (a-c) (the shadowed areas), in correspondence with the basically adapted range of 0.025-0.28.

5.

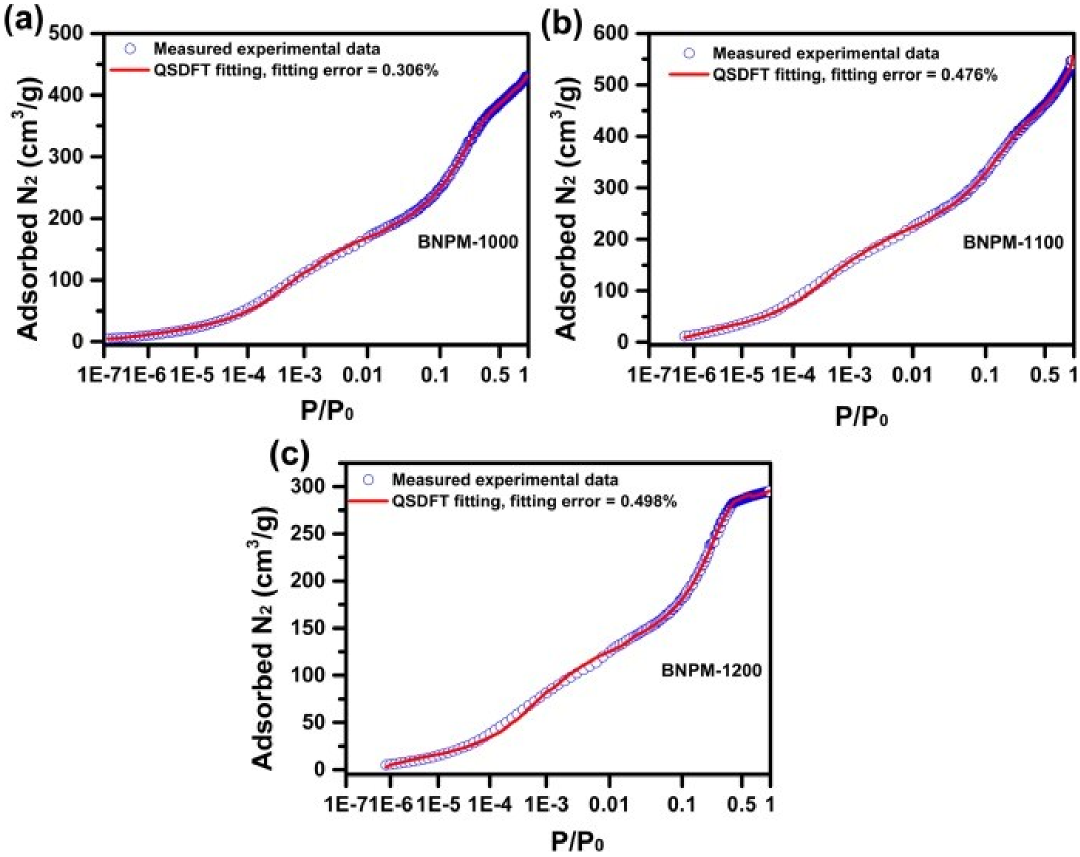

Figure S5. Comparison of experimental raw nitrogen isotherms and the theoretical isotherms evaluated based on the as-calculated QSDFT methods: a) sample BNPM-1000; b) BNPM-1100; c) BNPM-1200.

We utilized N_2-carbon adsorption model to simulate the pore distributions, including slit and cylinder pore geometry for micro-and meso-porous properties by using QSDFT as a calculation method. Among all the DFT models, such model displays the lowest fitting error (< 0.5%) and shows an agreement with the experimental data (see Figure S5). This QSDFT method takes into account the effects of surface heterogeneity and corrugated roughness of pore walls on the micro-/meso-porous materials [S5]. Based on the TEM and N_2-adsorption-desorption data and analysis in the main text, it is obvious that the QSDFT calculation model could be experimentally and theoretically agreeable to describe the BNPM samples.

6.

Table S1. Summary of porosity properties of BNPM-1000, BNPM-1100 and BNPM-1200

Samples	BET SSA (m^2/g)[a]	Tot. PV(cm^3/g)[b]	Mic. PV (cm^3/g)[c]	Mic. PV/Tot. PV (%)[d]	PSDs (nm)[e]
BNPM-1000	1149	0.680	0.412	60.6	0.9, 1.9
BNPM-1100	1406	0.887	0.535	60.3	0.9, 1.9
BNPM-1200	847	0.485	0.298	61.4	0.9, 1.9

[a]The Brunauer-Emmett-Teller specific surface areas (BET SSAs) are calculated by the seven-point BET method, with a selected pressure range in view of the corresponding Figure S4. [b]The total pore volume (Tot. PV) was obtained at P/P_0 to be of 0.997. [c]The corresponding micropore volumes (Mic. PV) were estimated by the QSDFT method model based on the N_2-adsorption isotherms. [d]The Mic. PV/Tot. PV is the proportion of the microporous volume amount to the total pore volume amount. [e]The pore size distributions (PSDs) were calculated by using the QSDFT model method.

7.

Table S2 Elemental compositions of BNPMs prepared.

Sample	B (at%)	N (at%)	O (at%)	C (at%)
BNPM-1000	43.7	39.3	16.9	0.1
BNPM-1100	47.6	47.4	4.9	0.1
BNPM-1200	48.7	48.5	2.7	0.1

The chemical composition of B was determined by a plasma optical spectroscopy (ICP-OES, Iris Adantage, Nippon Jarrell Ash Co., Japan). N content was determined by a sodium hydroxide melting distillation-neutralization titration method. C content was determined by a carbon/sulfur determinator (CS-444LS, LECO Co., USA) with the standard substance of $CaCO_3$ (501-034). O content was measured by an oxygen determinator (TC-436AR, LECO Co., USA) using Y_2O_3 as the standard substance. These chemical composition analyses indicate that, over 1100 °C, the BNPMs consist of a BN phase with B+N > 95 at %; and the B/N ratios are close to 1/1; a negligible carbon content, 0.1 at %; and less than 5 at % O content. It is believed that the real O contents in our BNPMs should be lower than the values measured in Table S1, because it is difficult to absolutely avoid adsorbing moistures due to an inevitable exposure of them to air atmosphere."

8.

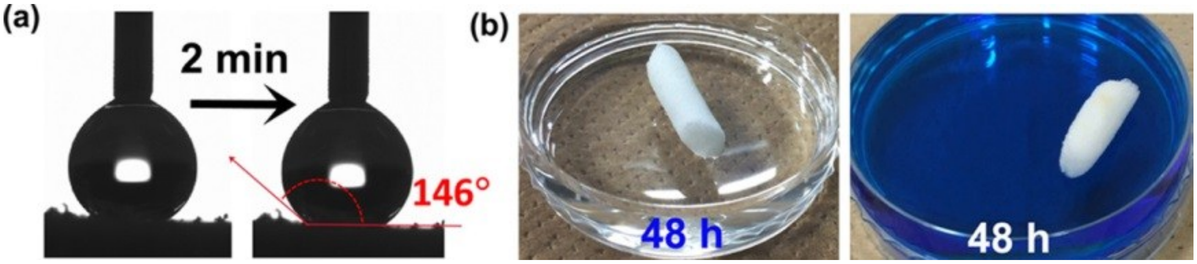

Figure S6. (a) Photograph of a water droplet on the surface of as-ground BNPM powder showing a contact angle of ~ 146°, thus hydrophobic properties. (b) The BNPM floating on the surface of pure water and dye aqueous solution (representative methyl blue solution) without solution infiltration for at least 48 hs.

9.

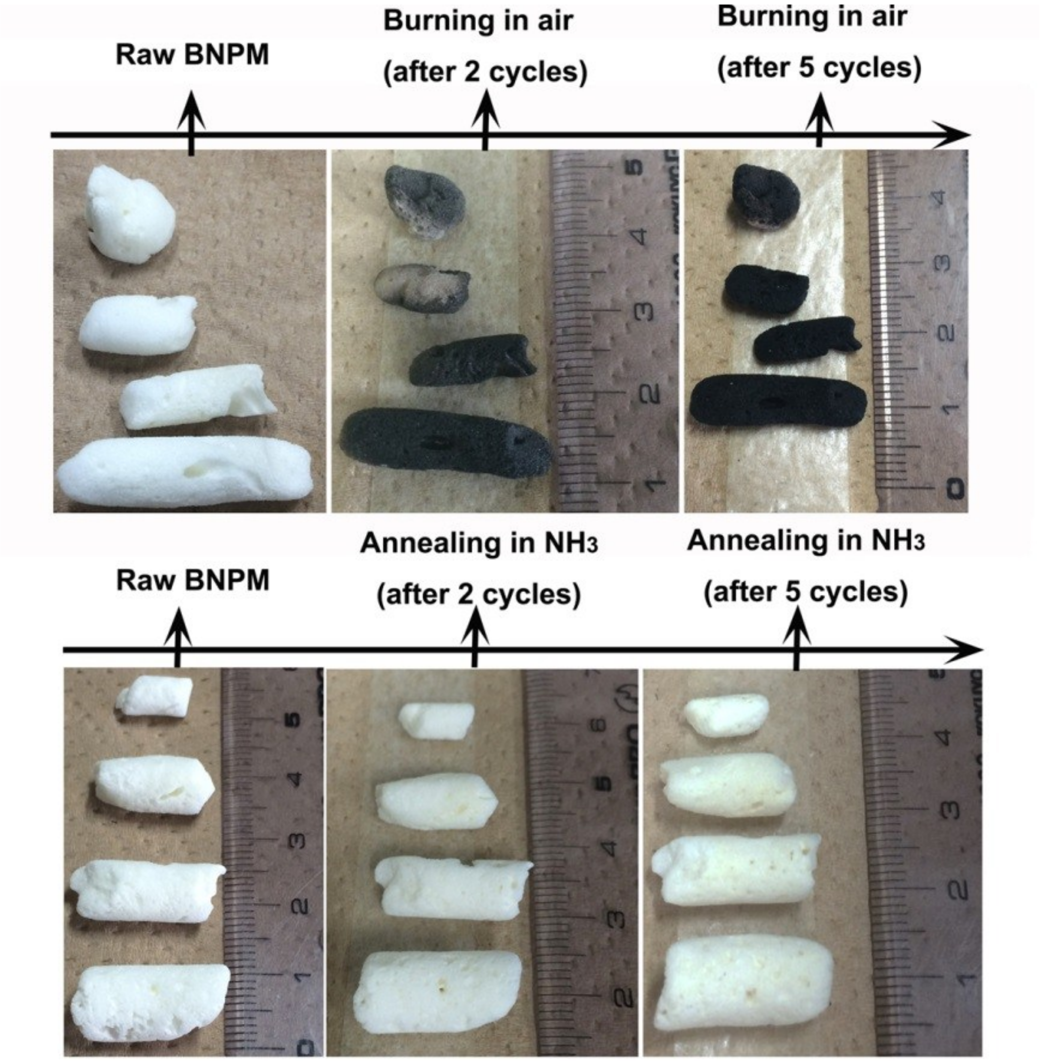

Figure S7. Photographs of BNPM-1100 after removal of the absorbed oil and burning in air followed by annealing in ammonia atmospheres at 900 °C for 1 h. It is obvious that the BNPM keeps its original monolithic shape after the oil-removal treatments. The body colors show corresponding differences.

10.

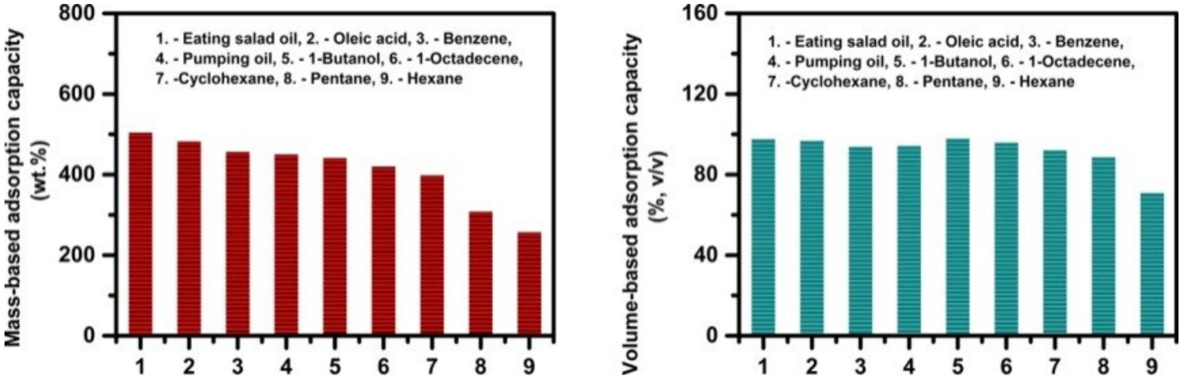

Figure S8. The mass-based and corresponding volume-based absorption capacities of different kinds of oils that usually float on the water surface at normal conditions. Using the presently developed BNPM-1100 samples, one may very fast reach the oil-saturated states for these ten kinds of water-floatable oils, and even to reach nearly saturated cases only within 10 s. Moreover, absorbed capacities are also very high.

11.

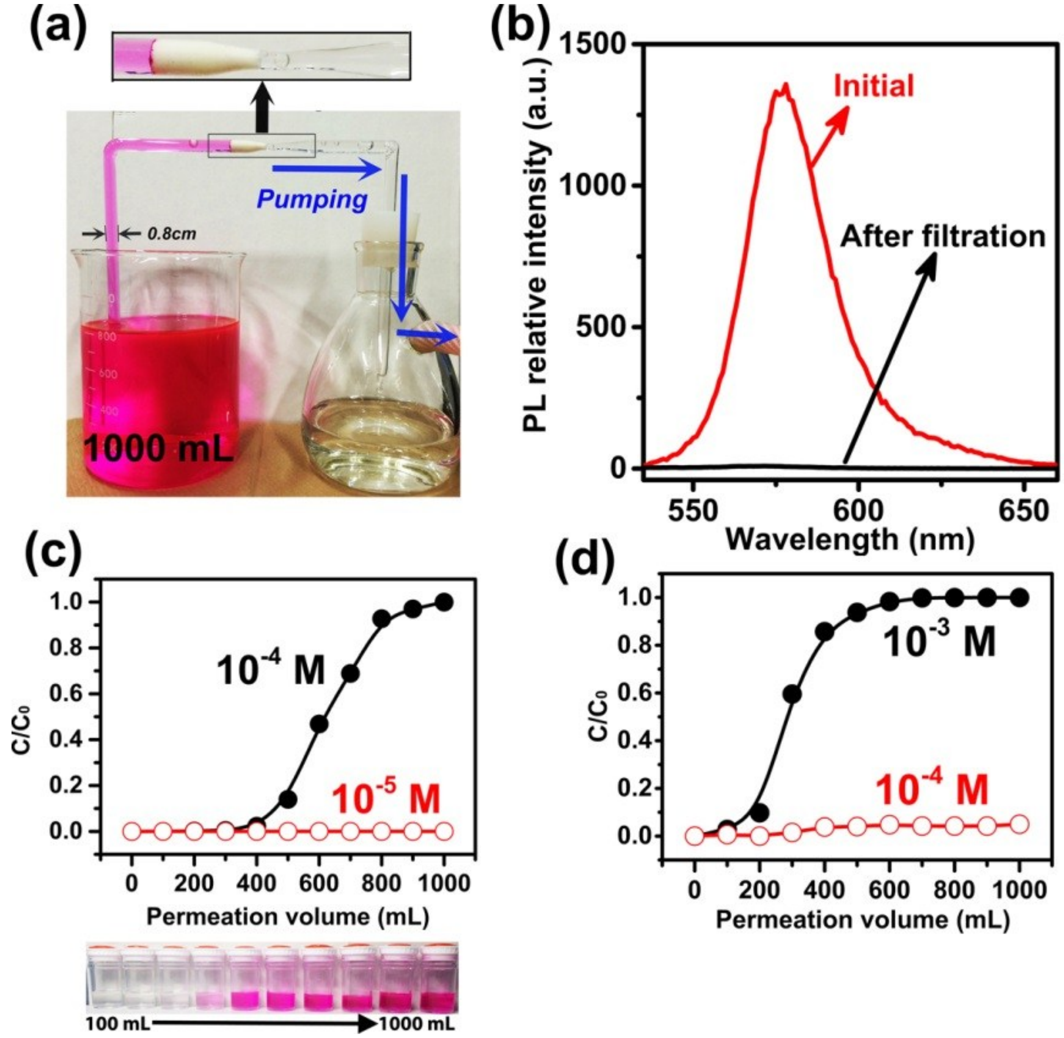

Figure S9. (a) Photograph of real filtration absorption by using a BNPM filtration column. (b) Photoluminescence spectra of the original RB (10^{-5}M) and its purified solution after purifying 1000 mL of RB solution by using the filtration device shown in (a). (c-d) Breakthrough curves for passage of different concentrations of RB and Cd(II) solutions (at pH=7.0) through the BNPM-1100 column with an identical weight of 50 mg, plotted based on the C/C_0 *vs* permeation volume (C is the outlet RB or Cd(II) solution concentrations, C_0 is the original concentration of these solutions). The bottom panel of (c) shows the color changes of the outlet RB solutions with every 100 mL (10^{-4}M) permeation.

12.

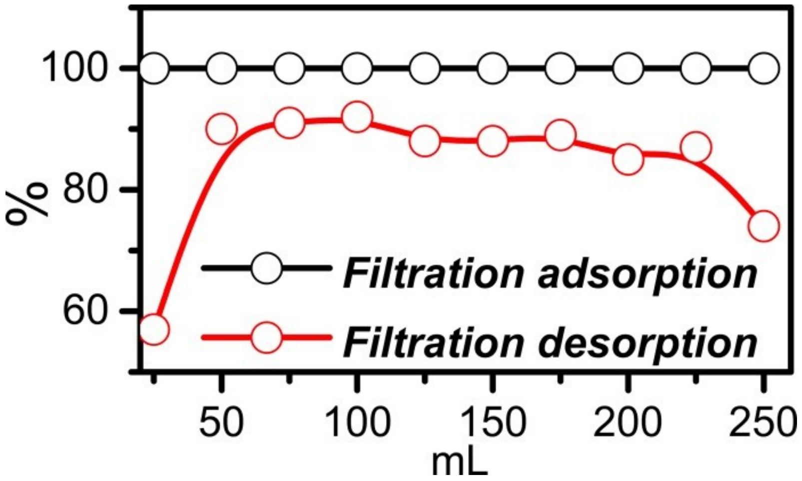

Figure S10. The consecutive adsorption-desorption ratio with every 25 mL RB solution for filtration adsorption and every 25 mL ethanol filtration desorption, at pH=7.0, using 10^{-3}M RB seed solutions. This figure corresponds to Figure 8c in the main text.

13.

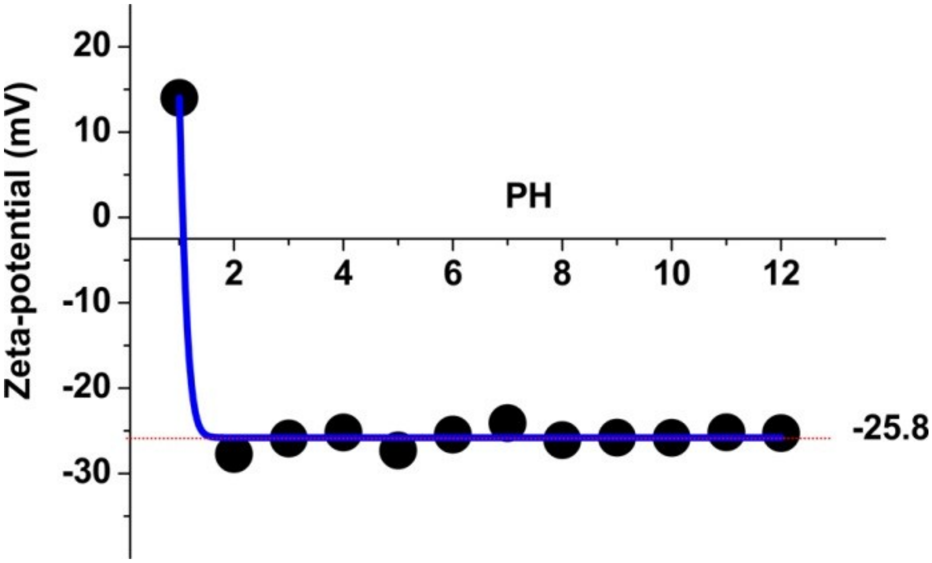

Figure S11. Zeta-potential measurements showing an overall negative surface charge at the condition of pH ≥ 2.

14.

Table S3. Comparisons of different adsorption performances of different BN-based adsorbents

BN-based adsorbents	*Absorption capacity*			*Ref.*
	Oils (wt.%, v%)[¥]	*Dye (mg/g)*	*Heavy metal ion (mg/g)*	
Nanosheet-structured BN spheres	780, --	MG[a] (324) MB[b] (233)	Cd(II) (107.0)	[S6]
Porous BN nanosheets /PVDF	300-900, --	/	/	[S7]
Activated BN	/	CR[c] (350) MO[d] (400)	Pb(II) (225)	[S8]
Porous BN whiskers	/	MO (298)	Cu(II) (373)	[S9]
BN nanocarpets	/	MB (272.4)	/	[S10]
Ultrathin-shell BN hollow spheres	/	BY[e] (191.7) MB (116.5)	/	[S11]
Functional 3D BN architectures	/	BY (424.3) CR (717.5)	/	[S12]
Ultrathin BN nanosheets	/	MB (436)	/	[S13]
BN ultrathin fibrous nanonets	/	MB (327.8)	/	[S14]
Graphene-like layered h-BN	/	GTF[f] (88.5)	/	[S15]
BN fibers	/	MB (392.2)	/	[S16]
Hierarchical porous BN	/	MB (263.1)	/	[S17]
Porous BN nanosheets	2000-3300, --	CR (782)	/	[S18]
3D BN foam scavengers	7000-19000, 13%-25%	MB (497) MO (461)	/	[S19]
Ultralight BN aerogels	16000, 12%	/	/	[S20]
BNPM-1100	258-505, 71%-98%	RB[g] (554)	Cd(II) (561)	This work

[a]Malachite green. [b]Methylene blue. [c]Congo red. [d]Methyl orange. [e]Basic yellow. [f]Fluoroquinolone antibiotic gatifloxacin.[¥] wt.% means the mass-based adsorption capacity, the v% is the corresponding volume-based adsorption capacity calculated as following [30]:

$$v\% = \frac{V_{oil}}{V_{absorber}} \times 100\%$$

$$= \frac{M_{oil}/\rho_{oil}}{M_{absorber}/\rho_{absorber}} \times 100\%$$

$$= \frac{M_{oil}}{M_{absorber}} \times \frac{\rho_{absorber}}{\rho_{oil}} \times 100\%$$

$$= N_{oil} \times \frac{\rho_{absorber}}{\rho_{oil}} \times 100\%$$

Table S4. Comparison of oil adsorption capacities of different adsorbent materials

Sorbent materials	*Adsorption capacity of oils (wt.%, v%)*	*Ref.*
Octadecyltrichlorosilane-coated polymerized octadecylsiloxane sponges	4200 - 6800, 35% - 60%	[S21]
Hydrophobicity-modified chitin sponges	3000 - 5800, 80% - 90%	[S22]
Carbon nanotube/polyurethane sponges	800 - 3490, 25% - 160%	[S23]
High internal phase emulsion xerogels	1510 - 3220, 150% - 326%	[S24]
Cellulose aerogel	1840 - 2050, 89% -- 101%	[S25]
Core-shell fluorinated-polyacrylate/ hydrophobic SiO_2 functionalized polyamide sponges	2500 - 6000, --	[S26]
Graphene oxide-coated cottons	1000 - 2500, --	[S27]
Ternary polyacrylate copolymer resin	1280-2300, --	[S28]
Nitrogen-rich/fire-resistance Carbon aerogels	500-1250, 75.5%-95.6%	[S29]
Nanowire-membrane	600-1900, 210%-600%	[S30]
Superhydrophobic/superoleophilic sponges	1200-1900, --	[S31]
Silica-modified polymeric monoliths	300-1700, 79% -- 268%	[S32]
Activated carbons	<100, --	[S33]
BNPM-1100	258 - 505, 71%-98%	This work

Table S5. Comparison of RB adsorption capacities of different adsorbent materials

Sorbent materials	Adsorption capacity of RB dye (mg/g)	Ref.
Commercial activated carbons	527	[S34]
Activated carbons	264	[S35]
Graphenes	201	[S36]
Mesoporous carbon fibers	469	[S37]
Ordered mesoporous carbons	215	[S38]
Porous graphitic carbon	67.9	[S39]
Kaolinites	46.1	[S40]
Fe_3O_4 nanoparticles	162	[S41]
Acid-heat activated rectorites	59.1	[S42]
Mesoporous magnesium silicate	190	[S43]
AIMCM-41	41.9	[S44]
Zeolites	6	[S45]
Sodium montmorillonites	42.2	[S46]
BNPM-1100	554	This work

Table S6. Comparison of adsorption capacities of Cd(II) ion for different adsorbent materials

Sorbent materials	Adsorption capacity of Cd(II) (mg/g)	Ref.
Commercial activated carbons	8	[S47]
Activated carbons	4.8	[S48]
Nitrogen-doped carbon nanofibers	161±5	[S49]
Mesoporous carbons	406.6	[S50]
Multi-walled carbon nanotubes	0.14	[S51]
B-doped g-C_3N_4	159.2	[S52]
Celluloses	83.6	[S53]
3D graphene oxide	234.8	[S54]
Alkaline deoxygenated grapheme oxide	156	[S55]
L-cysteine grafted nanoporous carbons	198	[S56]
Tetrasulfide-functionalized silica	22.3	[S57]
Zeolites	0.15	[S58]
BNPM-1100	561	This work

15.

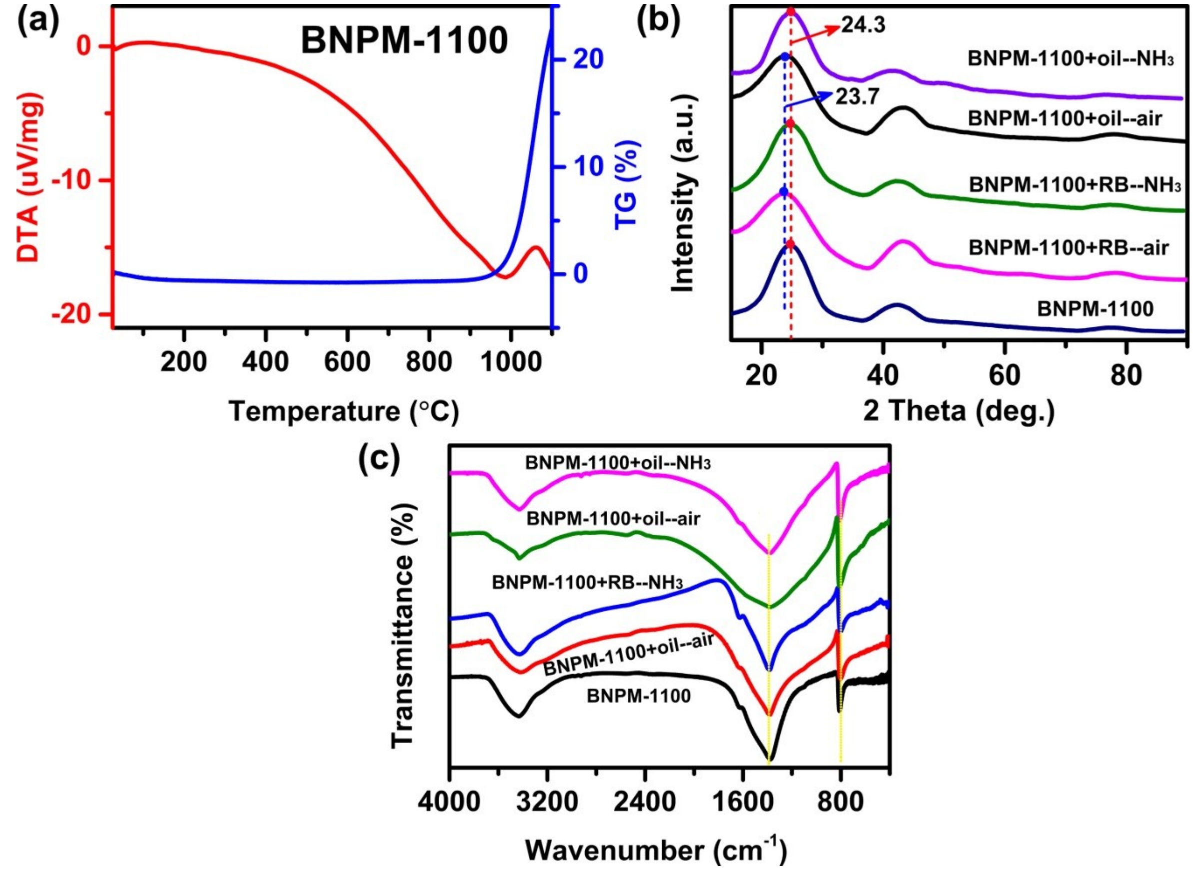

Figure S12. Studies of Stability of BNPMs. (a) TG-DTA curves of BNPM-1100 in air atmosphere with thermal ratio of 10 °C/min from 25 to 1200 °C. (b) XRD of samples regenerated under ammonia and air atmospheres from the BNPMs after their oil and RB adsorption. (c) FTIR spectra of samples regenerated under ammonia and air atmospheres from the BNPMs after their oil and RB adsorption.

16.

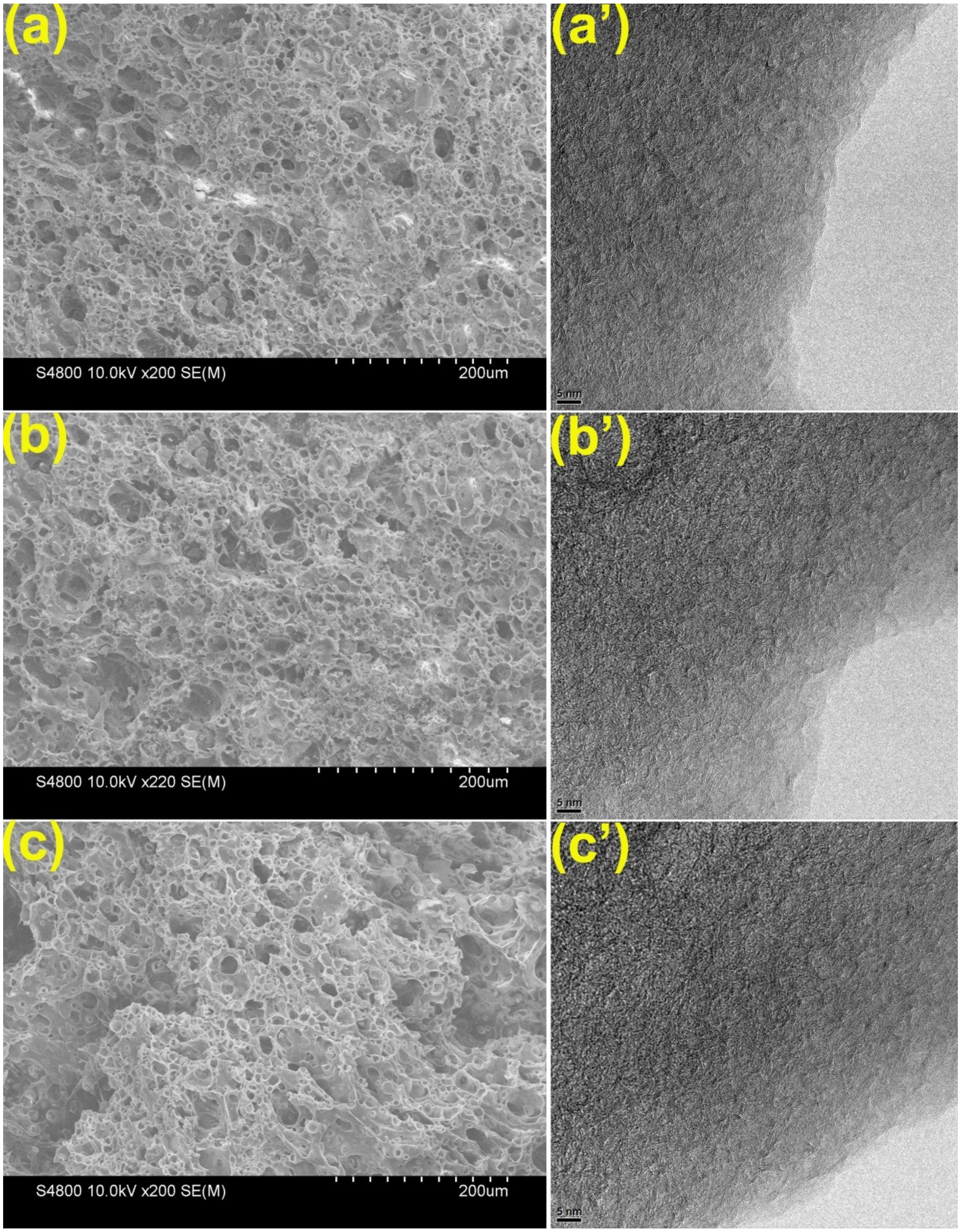

Figure S13. SEM and TEM images of the BNPM-1100, and regenerations of BNPM-1100 after oil and RB adsorption. (a) and (a') original BNPM-1100. (b) and (b') Regeneration of BNPM-1100 after oil adsorption subjected to high-temperature treatment with ammonia. (c) and (c') Regeneration of BNPM-1100 after RB adsorption subjected to high-temperature treatment with ammonia.

17.

Video SV1: Adsorption of soaking of a salad oil by using the obtained BNPM-1100 sample.

Video SV2: Filtration-adsorption removal of RB from its aqueous solution by using the designed device.

18.

References for Supporting Information

[S1]. Xue Y, Liu Q, He G, et al. Nanoscale Res. Lett. 2013, 8, 1-7.
[S2]. Thomas J, Weston N E, O'connor T E. J. Am. Chem. Soc. 1962, 84: 4619-22.
[S3]. Sumiya H, Iseki T, Onodera A. Mater. Res. Bull. 1983, 18: 1203-7.
[S4]. Zhao Z, Yang Z, Wen Y, et al. J. Am. Ceram. Soc. 2011, 94: 4496-501.
[S5]. Gor G Y, Thommes M, Cychosz K A, et al. Carbon 2012, 50: 1583-90.
[S6]. Liu F, Yu J, Ji X, et al. ACS Appl. Mater. Inter. 2015, 7: 1824-32.
[S7]. Yu Y., Chen H., Liu Y., *et al.* Adv. Mater. Interfaces 2015, 2: 1400267.
[S8]. Li J, Xiao X, Xu X, et al. Sci. Rep. 2013, 3: 3208.
[S9]. Li J, Lin J, Xu X, et al. Nanotechnology 2013, 24: 155603.
[S10]. Zhang X, Lian G, Zhang S, et al. CrystEngComm 2012, 14: 4670-6.
[S11]. Lian G, Zhang X, Zhang S, et al. Energ. Environ. Sci. 2012, 5: 7072-80.
[S12]. Liu D, Lei W, Qin S, et al. Sci. Rep. 2014, 4: 4453.
[S13]. Zhang S, Lian G, Si H, et al. J. Mater. Chem. A 2013, 1: 5105-12.
[S14]. Lian G, Zhang X, Si H, et al. ACS Appl. Mater. Inter. 2013, 5: 12773-8.
[S15]. Chao Y, Zhu W, Chen J, et al. Green Chem. Lett. Rev. 2014, 7: 330-6.
[S16]. Li J, Huang Y, Liu Z, et al. J. Mater. Chem. A 2015, 3: 8185-93.
[S17]. Maleki M, Beitollahi A, Javadpour J, et al. Ceram. Int. 2015, 41: 3806-13.
[S18]. Lei W, Portehault D, Liu D, et al. Nat. Commun. 2013, 4: 1777.
[S19]. Zhao H, Song X, Zeng H. NPG Asia Mater. 2015, 7: e168.
[S20]. Song Y, Li B, Yang S, et al. Sci. Rep. 2015, 5: 10337.
[S21]. Ke Q, Jin Y, Jiang P, et al. Langmuir, 2014, 30: 13137-42.
[S22]. Duan B, Gao H, He M, et al. ACS Appl. Mater. Inter. 2014, 6: 19933-42.
[S23]. Wang H, Wang E, Liu Z, et al. J. Mater. Chem. A 2015, 3: 266-73.
[S24]. Wu Y, Zhang T, Xu Z, et al. J. Mater. Chem. A 2015, 3: 1906-9.
[S25]. Nguyen S T, Feng J, Le N T, et al. Ind. Eng. Chem. Res. 2013, 52: 18386-91.
[S26]. Li K, Zeng X, Li H, et al. RSC Adv. 2014, 4: 23861-8.
[S27]. Sun H, Zhu Z, Liang W, et al. RSC Adv. 2014, 4: 30587-91.
[S28]. Fang P, Mao P, Chen J, et al. J. Appl. Polym. Sci. 2014, 131: 40180.
[S29]. Yang Y, Tong Z, Ngai T, et al. ACS Appl. Mater. Inter. 2014, 6: 6351-60.
[S30]. Yuan J, Liu X, Akbulut O, et al. Nat. Nanotechnol. 2008, 3: 332-6.
[S31]. Zhu Q, Pan Q, Liu F. J. Phys. Chem. C 2011, 115: 17464-70.
[S32]. Chen X, Liu L, Liu K, et al. J. Mater. Chem. A 2014, 2: 10081-10089.
[S33]. Lillo-Ródenas M A, Cazorla-Amorós D, Linares-Solano A. Carbon, 2005, 43: 1758-67.
[S34]. Hayeeye F, Sattar M, Tekasakul S, et al. Songklanakarin J. Sci. & Technol. 2014, 36: 177-87.
[S35]. Gad H M H, El-Sayed A A. J. Hazard. Mater. 2009, 168: 1070-81.
[S36]. Liu K, Li H, Wang Y, et al. Colloids Surf. A Physicochem. Eng. Asp. 2015, 477: 35-41.
[S37]. Dong Y, Lin H, Jin Q, et al. J. Mater. Chem. A 2013, 1: 7391-8.

[S38]. Zhuang X, Wan Y, Feng C, et al. Chem. Mater., 2009, 21: 706-16.
[S39]. Sun L, Tian C, Wang L, et al. J. Mater. Chem. 2011, 21: 7232-9.
[S40]. Khan T A, Dahiya S, Ali I. Appl. Clay Sci. 2012, 69: 58-66.
[S41]. Peng L, Qin P, Lei M, et al. J. Hazard. Mater. 2012, 209: 193-8.
[S42]. Xue X, He X, Zhao Y. Desalin. Water Treat. 2012, 37: 259-67.
[S43]. Zhu Y, Jian D, Wang S. Micro Nano Lett. 2011, 6: 671-4.
[S44]. Eftekhari S, Habibi-Yangjeh A, Sohrabnezhad S. J. Hazard. Mater. 2010, 178: 349-355.
[S45]. Jafari-zare F, Habibi-yangjeh A. Chinese J. Chem. 2010, 28: 349-56.
[S46]. Selvam P P, Preethi S, Basakaralingam P, et al. J. Hazard. Mater. 2008, 155: 39-44.
[S47]. Hydari S, Sharififard H, Nabavinia M, et al. Chem. Eng. J. 2012, 193: 276-82.
[S48]. Teker M, Imamoglu M, Saltabas O. Turk. J. Chem. 1999, 23: 185-91.
[S49]. Modi A, Bhaduri B, Verma N. Ind. Eng. Chem. Res. 2015, 54: 5172-8.
[S50]. Zeng G, Liu Y, Tang L, et al. Chem. Eng. J. 2015, 259: 153-60.
[S51]. Salam M A. Int. J. Environ. Sci. Techol. 2013, 10: 677-88.
[S52]. Tan G, Li Z, Yuan H, et al. Sep. Sci. Technol. 2014, 49: 1566-73.
[S53]. Liu J, Xie T H, Deng C, et al. Sep. Sci. Technol. 2014, 49: 1096-103.
[S54]. Wu S, Zhang K, Wang X, et al. Chem. Eng. J. 2015, 262: 1292-302.
[S55]. Liu J, Du H, Yuan S, et al. Water Sci. Technol. 2015, 71: 1611-9.
[S56]. Anbia M, Davijani A H. Chem. Eng. J. 2013, 223: 899-907.
[S57]. Fan H T, Wu J B, Fan X L, et al. Chem. Eng. J. 2012, 198: 355-63.
[S58]. Remenárová L, Pipíška M, Florková E, et al. Clean Technol. Envir. 2014, 16: 1551-64.